RSC Advances

ROYAL SOCIETY OF CHEMISTRY

www.rsc.org/advances

Very high power and excellent rate capability $LiFePO_4$ Nanorods were hydrothermally synthesized at lower temperature.

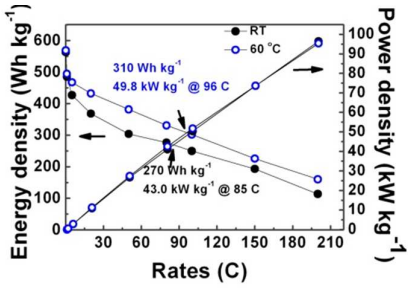

Small polarizations, i. e. good enough electronic and ionic conductivity is indispensible for high power lithium iron phosphate, especially for its applications to large current power supplies. Here, carbon coated $LiFePO_4$/C nanorods hydrothermally synthesized using Tetraglycol as surfactant followed by calcination exhibit very small polarizations (13.0 mV at 0.1 C, 1 C = 170 mA g^{-1}), high power densities (96.5 and 95.4 kW kg^{-1} at 200 C at RT and 60℃, respectively), and excellent cycling performance at high rates (92% discharge capacity retention at 100 C after 200 cycles) with only 10 wt% conductive additive. Intermixing between Fe and Li is detected in the as – synthesized, annealed and carbon coated samples. The superior rate capabilities (270.0 Wh kg^{-1} and 43.0 kW kg^{-1} at 85 C at RT, 310 Wh kg^{-1} and 49.8 kW kg^{-1} at 96 C at 60℃) and small polarizations are attributed to the nanoscale size along [010], the uniform carbon coating and the partial occupation of Li at the Fe site. The recipe in this study is quite simple, controllable, energy saving and readily up - scalable. The availability of very high power $LiFePO_4$ with excellent cycling capability at high rates will undoubtedly promote its applications to large current power supplies greatly such as electric and hybrid electric vehicles.

RSC advances

RSCPublishing

ARTICLE

Cite this: DOI: 10.1039/xoxxoooooox

Very High Power and Superior Rate Capability $LiFePO_4$ Nanorods Hydrothermally Synthesized Using Tetraglycol as Surfactant †

Ruiyuan Tian [a], Guangyao Liu [b], Haiqiang Liu [a], Lina Zhang [c], Xiaohua Gu [c], Yanjun Guo [a], Hanfu Wang [a],*, Lianfeng Sun [a],*, Weiguo Chu [a],*,

Received ooth January 20XX
Accepted ooth January 20XX

DOI: 10.1039/xoxxoooooox

www.rsc.org/

Small polarizations, i. e. good enough electronic and ionic conductivity is indispensible for high power lithium iron phosphate, especially for its applications to large current power supplies. Here, carbon coated $LiFePO_4$/C nanorods hydrothermally synthesized using Tetraglycol as surfactant followed by calcination exhibit very small polarizations (13.0 mV at 0.1 C, 1 C = 170 mA g^{-1}), high power densities (96.5 and 95.4 kW kg^{-1} at 200 C at RT and 60℃, respectively), and excellent cycling performance at high rates (92% discharge capacity retention at 100 C after 200 cycles) with only 10 wt% conductive additive. Intermixing between Fe and Li is detected in the as – synthesized, annealed and carbon coated samples. The superior rate capabilities (270.0 Wh kg^{-1} and 43.0 kW kg^{-1} at 85 C at RT, 310 Wh kg^{-1} and 49.8 kW kg^{-1} at 96 C at 60℃) and small polarizations are attributed to the nanoscale size along [010], the uniform carbon coating and the partial occupation of Li at the Fe site. The recipe in this study is quite simple, controllable, energy saving and readily up - scalable. The availability of very high power $LiFePO_4$ with excellent cycling capability at high rates will undoubtedly promote its applications to large current power supplies greatly such as electric and hybrid electric vehicles.

1、Introduction

Lithium iron phosphate is considered to be the most promising cathode material for lithium ion batteries, particularly those for electric and hybrid electric vehicles due to its good performance, low cost, environmental friendliness and safety etc. [1-3] High power density is indispensible for its applications to large current power supplies, which can be achieved provided that sufficiently high discharge voltages at high rates can be maintained, i. e. sufficiently small polarizations with both good electronic and ionic conductivities are necessary. [4 – 7] However, what is more often seen is that $LiFePO_4$ with high capacities at high rates usually shows relatively low discharge voltages, accompanied by large polarizations. [8-11] High discharge voltages of $LiFePO_4$ with small polarizations may be closely coupled to its structure, chemical composition, size, morphology and reaction pathways upon Li^+ insertion and extraction. [12-16] Up to now, the pursuit of high power $LiFePO_4$ is still far from satisfactory, and the correlation between high power and diversified materials parameters must be intensively explored.

Many methods have been tested to improve the electrochemical performance of $LiFePO_4$ by tailoring its structure, morphology and size to develop high capacities at high discharge rates. [17-20] Reducing polarizations by improving both electronic and ionic conductivities will increase its power density. However, small polarizations may have a significant influence on capacity but they don't necessarily result in high capacities. This is probably related to a match between ionic and electronic conductivities. It is actually quite difficult to obtain $LiFePO_4$ with both high energy and power densities. [21] Generally, perfect crystal is always desired for $LiFePO_4$ because diversified defects, such as the partial occupation of Fe at the Li site due to the blocking effect of Fe in the channel would degrade its electrochemical performance. [22–28] However, the doping of supervalent cations into the Fe site of $LiFePO_4$ was observed experimentally to benefit its electrochemical performance although this is theoretically controversial. [29-31] Thus, the presence of different cations at the Li and Fe sites seems to have opposite effects on the electrochemical performance of $LiFePO_4$. To the best of our knowledge, little is known about the doping of Li at the Fe site in $LiFePO_4$, i. e. so-called self - doping, and its dependence of the electrochemical performance.

We used a low temperature hydrothermal method at 140 ℃ to synthesize $LiFePO_4$ with tetraglycol as surfactant, followed by a carbon coating at 600℃ for 3 h with glucose as a carbon source in order to realize so-called self-doping. The partial occupation of Fe at the Li site and of Li at the Fe site was indeed observed in as-synthesized, annealed and carbon coated $LiFePO_4$ nanorods. In spite of the antisite defects, $LiFePO_4$ nanorods synthesized using this simple, controllable and up - scalable approach exhibit the highest power densities (high discharge voltages) for the same rates reported so far and superior rate capability (certain capacities still available at very high rates such as 200 C). This is extremely important for promoting the applications of $LiFePO_4$ in fields such as electric and hybrid electric vehicles.

ARTICLE

RSC advances

2. Experimental

Synthesis of $LiFePO_4$ Nanorods

Tetraglycol and deionized water in a volume ratio of 80:20 were mixed as the reaction medium throughout the hydrothermal preparation of $LiFePO_4$ nanorods. Typically, 5 ml of 1 M H_3PO_4 aqueous solution was mixed with 120 ml of tetraglycol, and then 15 ml of 1 M aqueous LiOH was slowly introduced during mechanical stirring and a white suspension was obtained. Finally, 10 ml of 0.5 M $FeSO_4$ solution was added with stirring, resulting in green suspension. All of this was completed in an inert atmosphere (Ar). The resulting mixture was transferred into a 200 ml Teflon-lined stainless steel autoclave which was sealed and heated to 140℃, and kept for 24 h, then cooled to room temperature (RT). The precipitate was centrifuged, washed with water and ethanol for several times, and dried in a vacuum desiccator at 80℃ for 12 h. The as synthesized samples (Sample S) were treated without (Sample H) and with glucose (20 wt.%) as the carbon source (Sample G), respectively at 200℃ for 0.5h, followed by annealing at 600℃ for 3h in Ar atmosphere.

Structural characterizations

The structures of samples S, H and G were characterized by X-ray diffraction technique (XRD). The XRD data were collected on a Rigaku D/MAX-2500 diffractometer with a Cu Kα radiation at 45 kV and 250 mA. A step scan mode was adopted with a step size of 0.02°, a sampling time of 1 s and an angle range of 15 - 130°. The morphology and structure of samples was studied by transmission electron microscopy and high resolution transmission electron microscopy (TEM, HRTEM, Tecnai F20, FEI Company, USA). The carbon content of sample G was determined using a carbon and sulfur analyzer (CS-344, LECO Company, USA).

Electrochemical measurements

Electrochemical experiments were performed using CR 2025 coin cell. The samples with and without coated carbon, acetylene black and PVDF (poly (vinylidene fluoride)) were mixed and ground with a weight ratio of 80:10:10 using a N-methyl-2-pyrrolidone (NMP) as the solvent. The resulting slurry was spread onto an aluminum foil and dried under vacuum at 110 ℃ for 12 h. The foil was punched into a circular disc and pressed under 20 MPa to from a cathode. The loading of active material is about 2.0 mg cm^{-2}. A lithium metal as the counter electrode and Celgard 2316 as the separator were used to assemble cells in an argon-filled glove box. 1.0 M $LiPF_6$ was dissolved in a mixture of ethylene carbonate (EC), ethyl methyl carbonate (EMC) and dimethyl carbonate (DMC) with a volume ratio of 1:1:1 as the electrolyte. Electrochemical experiments were carried out on a battery test system (BTS–5 V, Neware Company, China) at RT and 60℃. Electrochemical impedance spectra (EIS) were recorded using an electrochemical workstation (CHI660D, Shanghai Chenghua Company, China).

3. Results and Discussion

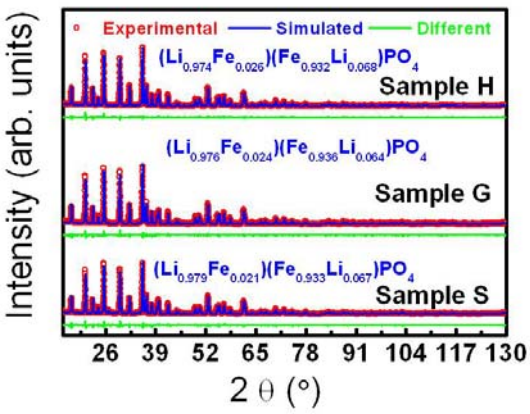

Figure 1. Experimental, simulated and different XRD patterns of sample S, H and G.

Figure 1 shows XRD patterns of samples S, H and G. From their XRD patterns sample H and G are found to be composed of single phase $LiFePO_4$ whereas sample S has some minor impurities. A model of an orthorhombic structure with space group of Pnma was employed to perform Rietveld refinements on the XRD data. 32 The simulated patterns based on the above structural model agree very well with the experimental ones. The refined parameters are outlined in Table 1 and Table S1 (Supporting Information). One can find that the annealing causes the lattice

Table 1. Parameters for Rietveld refinement for sample S, H and G.

Parameters \ Sample		S	H	G
a (Å)		10.3215	10.3134	10.3163
b (Å)		5.9947	5.9998	6.000
c (Å)		4.6960	4.6932	4.6923
Size of crystallites (nm)	(200)	58.0	64.0	60.0
	(101)	104.3	92.7	86.3
	(020)	53.8	74.5	72.0
Reliability factors	R_{wp}	8.08%	7.13%	7.82%
	R_B	2.31%	1.93%	2.09%
	S	1.440	1.261	1.404
Refined formula		$(Li_{0.979}Fe_{0.021})(Fe_{0.933}Li_{0.067})PO_4$ $Li_{1.046}Fe_{0.954}PO_4$	$(Li_{0.974}Fe_{0.026})(Fe_{0.932}Li_{0.068})PO_4$ $Li_{1.042}Fe_{0.958}PO_4$	$(Li_{0.976}Fe_{0.024})(Fe_{0.936}Li_{0.064})PO_4$ $Li_{1.040}Fe_{0.960}PO_4$
Impurity percentage		4.24%	-	-

to contract along both a and c but expand along b (Table 1). This may be a consequence of the stress relief upon annealing. The sizes of crystallites along the directions normal to (200), (101) and (020) are estimated according to the Scherrer equation, $d=k\lambda/\beta\cos\theta$ in which λ is the wavelength, k a constant, 0.89, β the full width at half height and θ is the Bragg angle by taking the instrument broadening effect into considerations.[33] The comparable sizes along the directions normal to (200) and (020) are much smaller than that along the direction normal to (101), suggesting a rod-like morphology. According to the Rietveld refinements the formulae were derived to be $(Li_{0.979}Fe_{0.021})(Fe_{0.933}Li_{0.067})PO_4$ $(Li_{1.046}Fe_{0.954}PO_4)$, $(Li_{0.974}Fe_{0.026})(Fe_{0.932}Li_{0.068})PO_4$ $(Li_{1.042}Fe_{0.958}PO_4)$, and $(Li_{0.976}Fe_{0.024})(Fe_{0.936}Li_{0.064})PO_4$ $(Li_{1.040}Fe_{0.960}PO_4)$ for samples S, H and G, respectively. The Li site is found to be occupied by around 3% Fe, and the Fe site by around 7% Li for all samples. In fact, we also tried the models with Li replaced by vacancies

RSC advances ARTICLE

to refine the XRD data, giving a little higher values of figure of merit, i.e. 1.27 versus 1.26 for sample H and 1.41 versus 1.40 for sample G. The very small differences are due to the small capability of Li scattering X-ray. This further supports the intermixing between Fe and Li. In addition, we performed the valence calculation of elements at different sites according to two models: bond valence sum and charge distribution model.[34,35] The valences for the identical elements at the same sites derived from two models are very comparable (Table S1, Supporting Information), supporting the Rietveld refinement results. Around 3% Fe occupation at the Li site is consistent with the values reported.[36,37] The occupation of about 7% Li at the Fe site is also reasonable in that the Fe_{Li} and Li_{Fe} defect couples are not only energetically favorable but their concentrations are independent on one side,[38 - 41] and the ionic radii for Li^+ and Fe^{2+} are very close as well (Li^+: 0.76 Å and Fe^{2+}: 0.78 Å) on the other side. In fact, the partial occupation of Li at the Fe site and the excess of Li in the formula were also reported.[42 – 44] The annealing of the samples with and without glucose as carbon source at 600℃ for 3 h has no sizable effect on the ordering of Fe and Li, at variance with Ref. [45].

To further prove the intermixing between Li and Fe, RT Mössbauer spectra and temperature dependence of magnetic susceptibility of sample G were acquired, as shown in Figure 2 (a) and (b), respectively. The spectrum was simultaneously analyzed in terms of two components labeled Fe^{2+} and Fe^{3+} in Figure 2 (a). The corresponding hyperfine parameters are outlined in Table 2. The isomer shifts and quadrupole splittings for both Fe^{2+} and Fe^{3+} are close to those reported in Refs. 46, 47, which are assigned to Fe^{2+} in $LiFePO_4$ and Fe^{3+} due to lattice defects in $LiFePO_4$ such as the replacement of Li by Fe instead of Fe^{3+} from other impurities, respectively. The difference lies in a higher ratio of Fe^{3+} to Fe^{2+} doublet areas, i. e. around 20% versus 10% reported in Ref. 46. The presence of Fe^{3+} due to lattice defects is also strongly supported by the perfectly linear dependence of magnetic susceptibility on temperature above the Neel temperature of about 50K in Figure 2 (b). [48] If around 20% Fe^{3+} arises from other impurities in the sample, one should undoubtedly be able to observe some traces from the dependences of magnetic susceptibility on temperature. [48] According to the Curie-Weiss law, the effective moment of Fe in sample G was derived to be 5.62 μB, which is quite comparable to 5.36 μB due to the replacement of Li by Fe. [49] All of this, along with the XRD refinement results gives strong evidence for the partial occupation of the Li site by Fe and of the Fe site by Li.

TEM images, HRTEM images, along with their corresponding Fast Fourier Transformation (FFT) images for three samples are shown in Figure 3 a-c and d-f, respectively. The size of $LiFePO_4$ nanorods for three samples is found to have a bit broad distributions. $LiFePO_4$ nanorods are found to coalesce and spheroidize subject to the annealing at 600 ℃. The combination of HRTEM and corresponding FFT images allows one to determine the crystallographic directions of a nanorod, i. e. one of the shorter axes of nanorods is along [010], being consistent with the results of size estimate from XRD (Table 1). The corners of nanorods are rounded, and a relatively uniform and thin layer of carbon with thickness of about 4 nm is coated on $LiFePO_4$ nanorods for sample G. In contrast, no carbon thin layer was observed for samples S and H. This indicates the thin layer of carbon for sample G results from the added glucose.

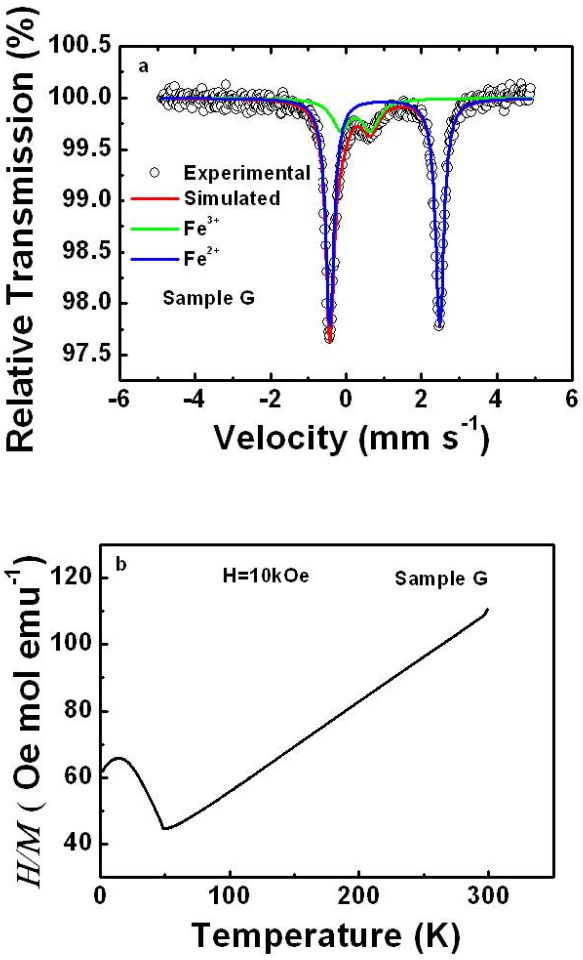

Figure 2. Mossbauer spectrum (a) and magnetic susceptibility (b) for sample G

Table 2. Mössbauer parameters of sample G, Q_s is the electric quadrupole splitting value, δ is the isomer shift value, Γ is the peak width

Sample		δ (mm s^{-1})	Q_s (mm s^{-1})	Γ (mm s^{-1})	Area Ratio (%)
G	Fe^{2+}	1.11 ± 0.00	2.91 ± 0.00	0.13±0.00	78.6
	Fe^{3+}	0.34± 0.00	0.78 ± 0.01	0.28±0.01	21.4

The electrochemical properties of sample H and G were measured, and their charge and discharge curves as well as corresponding coulombic efficiencies and discharge capacities at various rates at RT and 60℃ are shown in Figure 4. Both samples show high coulombic efficiencies at all charge and discharge rates, indicative of good reversible extraction / insertion of Li ions even at very high rates. At 0.1 C sample H and G exhibit 150.5 and 160.2 mAh g^{-1}, respectively. Sample G shows well defined discharge plateaus for different rates. Even for a rate of 200 C sample G still has a discharge capacity of about 38.0 mAh g^{-1} with an apparent voltage plateau, suggesting a superior rate capability and little contribution from the capacitor-like discharge capacity. This is very important for large current power supplies, especially for those requiring high discharge voltages such as electric and hybrid electric vehicles. In contrast, sample H is able to simply discharge at 20 C. Even so, in the case of no carbon coating, the rate capability of sample H is still far better than that in ref. 50, and even comparable to the carbon coated samples with an additive of 25

ARTICLE

RSC advances

wt% carbon black. [51] Again, the discharge capacities of both sample H and G at 60℃ are significantly higher than those at RT, especially for high rates. The discharge capacity of sample G for the rate of 200 C increases from 38.0 mAh g^{-1} at RT to 58.0 mAh g^{-1} at 60℃, an increase of 52.6%. Likewise, sample H shows an increase of 230% from 11.6 mAh g^{-1} at RT to 38.0 mAh g^{-1} at 60℃ for 20 C, and even 27.0 mAh g^{-1} for 30 C. The significant increase in discharge capacity for both samples is due to a decrease of Li^+ diffusion impedance which can be ascribed to a lattice expansion of $LiFePO_4$ at high temperatures.

Figure 3. TEM images (a) – (c), HRTEM images (d) – f) and FFT images of sample S, H and G. $LiFePO_4$ is rod-like in nanoscale, and one of the shorter axes is along [010], favoring the Li^+ diffusion

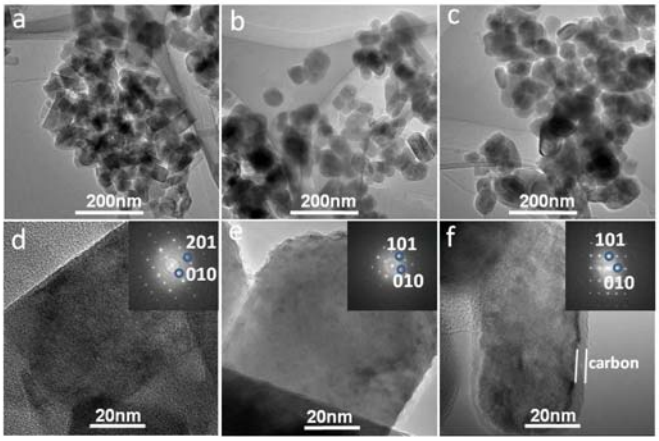

Figure 4. Charge and discharge curves and corresponding coulombic efficiencies at various rates of sample H (a) and G (b), and discharge capacities (c)

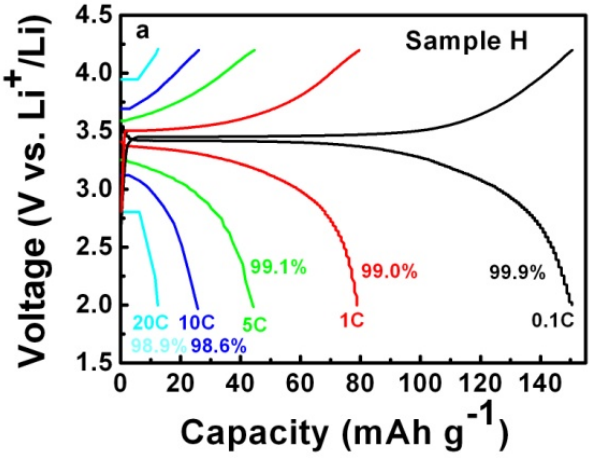

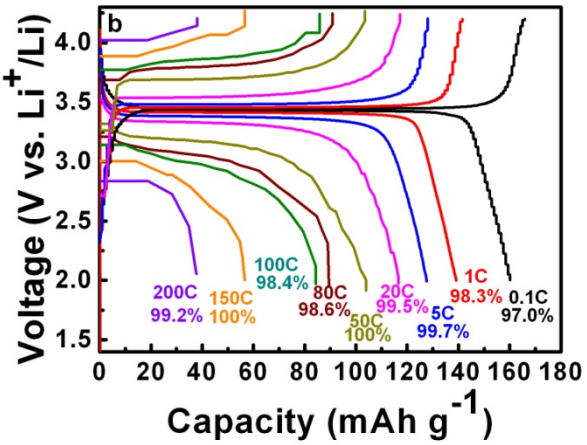

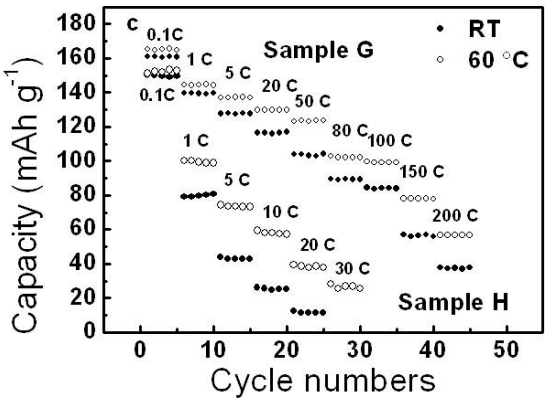

The rate dependences of the polarization and discharge voltage at 50% depth of discharge (DOD) are plotted in Figure 5. It is worthwhile to point out that the polarizations for sample G are very small, say 13.0 mV at 0.1 C, far smaller than 45.6 mV for the carbon-nanotube-decorated nano $LiFePO_4$ with very good performance.52 Sample H shows a polarization of about 96.0 mV at 0.1 C, far smaller than 310.0 mV at 0.1 C even with a little bit higher discharge capacity, 162 mAh g^{-1}. [53] Most strikingly, in this study the discharge voltages at 50% DOD, especially at high rates are very high, implying high power densities. The discharge voltages at 50% DOD for 0.1 and 200 C rates at RT for sample G are 3.434 and 2.837 V, respectively. The value of sample G at 200 C here is even higher than those at far lower rates, say 2.5 V at 80 C,[54] and very comparable to 2.87 V at 10 C with excellent rate performance. [55] The discharge voltages of sample H for 0.1 and 20 C at RT are 3.371 and 2.694 V, respectively, which are higher than 3.20 V [50] and 3.22 V [53] for 0.1 C, and 2.32 V for 20 C. [50] The excellent rate capability of sample G is very comparable to the best ones so far but the discharge voltages are far higher than those (Figure S1, Supporting Information).

Figure 6 shows both energy and power densities for sample G at RT and 60℃. Energy and power densities of sample G are 310.0 Wh kg^{-1} and 49.8 kW kg^{-1} at 96 C at 60℃, and 270.0 Wh kg^{-1} and 43.0 kW kg^{-1} at 85 C at RT, which are far higher than 227.0 Wh kg^{-1} and 34.0 kW kg^{-1} at 80 C at RT reported recently with a higher percentage of conductive additive (15 wt%). [54] At the rate of 200 C, a power density as high as 96.5 kW kg^{-1} was achieved, which is higher than 90 kW kg^{-1} reported with 65 wt%

RSC advances ARTICLE

conductive additive. [56] So high power densities due to high discharge voltages are of great significance for applications to electric and hybrid electric vehicles. The high discharge voltages at high rates at 50% DOD can be attributed to small polarizations.

Figure 5. Polarizations (a) and discharge voltages (b) at 50 % DOD for various rates of sample H and G, noting high discharge voltages

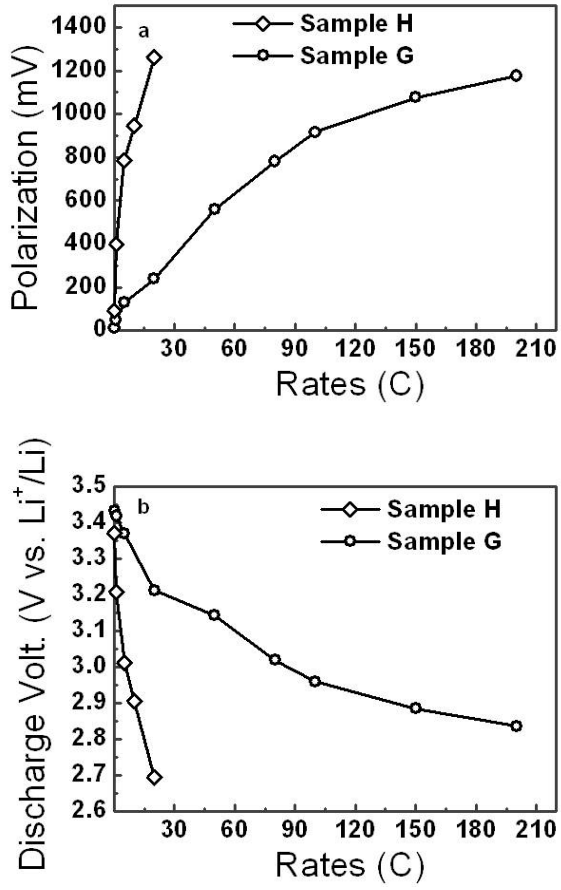

Figure 6. Power and energy densities at different rates for sample G at RT and 60℃

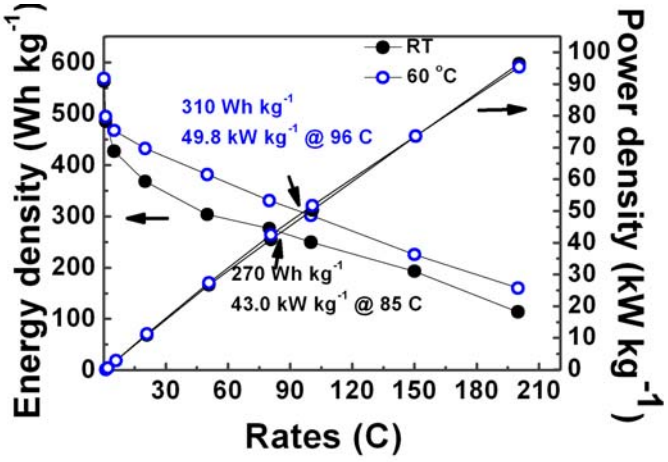

The cycling performances of sample H and G at different rates at RT and 60℃ are shown in Figure 7. Sample H has discharge capacity retentions of about 88% and 93% after 200 cycles at 1 and 5C at RT, and 79% and 76% at 60℃, respectively. Sample G shows high discharge capacity retentions, such as 80 % at 50 C and 77% at 100 C at 60 ℃, and 94% at 50 C and 97% at 100 C at RT after 200 cycles. Sample G is revealed to have excellent cycling performance at high rates, especially at RT.

Figure 7. Cycling performance at different rates for sample H and G at RT and 60℃

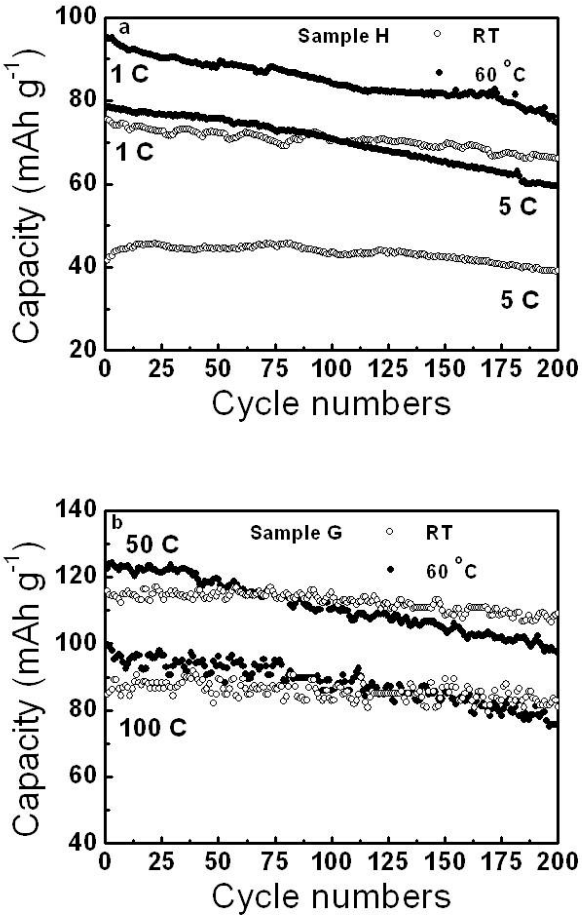

To estimate the resistance of sample H and G, their electrochemical impedance spectra (EIS) were acquired in Figure 8. A depressed semicircle and a sloping line are observed in the high- and low-frequency range, respectively for both samples. This clearly shows the features of the ohmic resistance, charge transfer resistance, and the Warburg behavior for both samples. According to the fundamental electrochemical process for lithium ion cells,[57] an equivalent circuit model is proposed and their simulated spectra are shown Figure 8 (a). In the model, R_s is the resistance of the electrolyte and electrode, R_1 and CPE_1 the resistance and capacity of the surface film, R_2 and CPE_2 the charge transfer resistance and capacity, and Z_w is the Warburg impedance. Also， the relationships of the impedance versus $\omega^{-1/2}$ for two samples are depicted in Figure 8 (b) to figure out their diffusion coefficients of Li^+. [58] Sample H is found to have far larger resistance and

ARTICLE

RSC advances

lower diffusion coefficient of Li^+, compared to sample G (Table 3). The diffusion coefficient of Li+ for sample H is estimated to be 2.65×10^{-16} cm^2 s^{-1} whereas that for sample G, 1.40×10^{-14} cm^2 s^{-1}, comparable to the values reported. [59, 60] It is apparent that much higher resistances and lower Li^+ diffusion coefficient are responsible for much worse electrochemical performance of sample H. The diffusion coefficient of Li^+ of two orders of magnitude lower for sample H revealed by the EIS is actually coupled to its much higher film and charge transfer resistances. Therefore, carbon coating not only plays a crucial role in the formation of solid electrolyte interface (SEI) films and thus SEI film resistance and charge transfer resistance but also in the diffusion of Li^+ which is significantly influenced by the electronic conductivities. Even so, sample H still shows better performance among samples without coated carbon as mentioned above. This implies better electronic conductivities of $LiFePO_4$ nanorods themselves involved in sample H.

Figure 8. Experimental and simulated impedance spectra of sample H and G

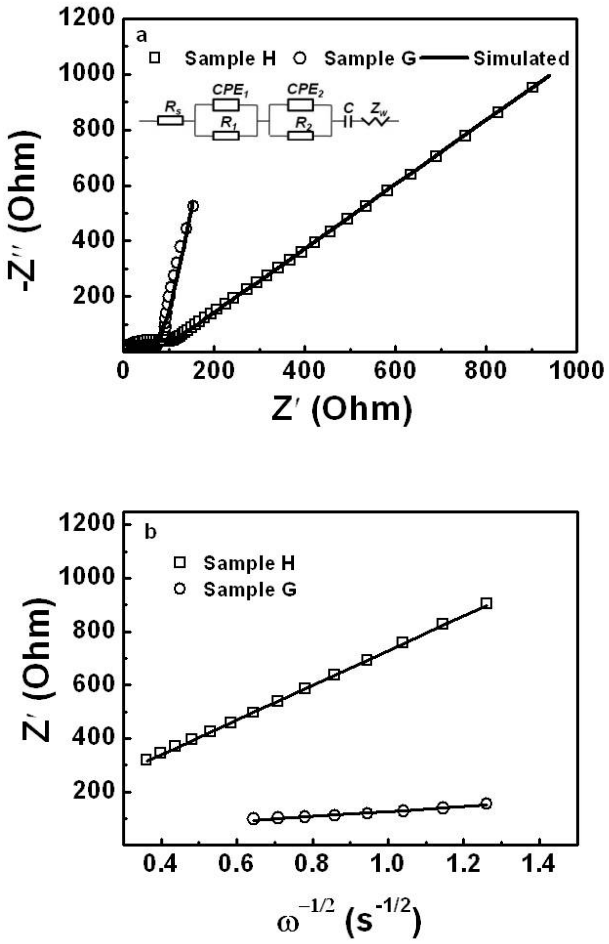

Table 3. Resistances derived from EIS based on the proposed circuit model and the diffusion coefficients of Li^+ for sample H and G

Samples	R_s (Ω)	R_1 (Ω)	R_2 (Ω)	D (cm^2s^{-1})
H	2.80	92.00	279.60	2.65×10^{-16}
G	0.80	1.06	59.88	1.40×10^{-14}

It is generally recognized that the anti-site defects in $LiFePO_4$, especially, the occupation of Li by Fe are considered to deteriorate its electrochemical properties due to the blocking effect of Fe in the channels upon Li^+ insertion and extraction. However, both sample H and G reported here have better electrochemical performance, especially higher power densities compared to those samples without and with coated carbon, respectively, which appears to contradict this recognition. Then, there may be some ways to realize the excellent rate capability and high power of sample G in the presence of Fe-Li antisite defects. i) Fe is not distributed uniformly in the Li channels, rather segregated in a few channels, and thus the antisite defect has no significant influence on the performance.[41, 61, 62] ii) A rearrangement of local structure takes place through the site exchange of Fe at the Li site and Li at the Fe site during charging, especially at a low rate. As a consequence, the Fe_{Li} defects would be finally removed. [63] iii) The negative effect caused by the Fe at the Li site is counteracted by the positive effect arising from the doping of Li into the Fe site, i. e. so-called self-doping, by increasing the number of polarons in LiFePO4. [64] Therefore, the superior rate capability and high discharge voltages of sample G at high rates can be ascribed to not only the nanoscale size along [010] and the uniform carbon coating of $LiFePO_4$ nanorods but the partial occupation of Li at the Fe site. For sample H without coated carbon, the interplay of the nanoscale size along [010] and the partial occupation of Li at the Fe site is responsible for the relatively better electrochemical performance. The nanoscale rods of $LiFePO_4$ formed as a result of tetraglycol as surfactant. The high viscosity of tetraglycol not only determines the morphology and size of $LiFePO_4$ but also influences the diffusion processes and kinetics of all chemical species involved in the reactions, and thus the formation of the Fe-Li antisite defects at certain temperature. Thus, it is probable to optimize the electrochemical performance of $LiFePO_4$ by suppressing the occupation of Fe at the Li site and maintaining the moderate occupation of Li at the Fe site through controlling the synthesis recipes carefully, such as the content of tetraglycol, temperature, reaction time etc. Therefore, this study opens up a way to enhance the electrochemical performance of $LiFePO_4$ by incorporating a certain amount of Li into the Fe site. Further investigations on the precise control of defects are under way.

4. Conclusions

High power and superior rate capability $LiFePO_4$ nanorods were synthesized via the hydrothermal method with tetraglycol as a surfactant at a temperature as low as 140 ℃, followed by the carbon coating with glucose as carbon source. The high viscosity of tetraglycol plays a key role in the morphology and size of $LiFePO_4$ and the formation of Fe-Li antisite defects. About 3 % Fe_{Li} and 7 % Li_{Fe} antisite defects are present in the as-synthesized, annealed and carbon coated $LiFePO_4$, and the Fe_{Li} antisite defects don't deteriorate its superior electrochemical capability. The excellent rate capability and small polarizations result from not only the nanoscale size along [010] and the uniform carbon coating of $LiFePO_4$ nanorods but also the partial occupation of Li at the Fe site. Very high power densities due to high discharge voltage, such

RSC advances ARTICLE

as 95.4 and 96.5 kW kg^{-1} at 200 C at RT and 60℃ with only 10 wt% conductive additive, respectively are achieved, and superior rate performances, such as an energy density of 270.0 Wh kg^{-1} and 43.0 kW kg^{-1} at 85 C at RT, 310 Wh kg^{-1} and 49.8 kW kg^{-1} at 96 C at 60℃ are also available. 95% and 92% discharge capacity retentions after 200 cycles at the charge and discharge rates of 50 and 100 C for the carbon coated $LiFePO_4$/C nanorods with glucose as carbon source are obtained. This work develops a simple, controllable and up - scalable recipe for synthesizing very high power $LiFePO_4$ nanorods with superior rate capability by using a suitable surfactant and coating carbon with proper carbon sources. We anticipate that this work will stimulate the pursuit of high power $LiFePO_4$, particularly, the availability of the excellent cycling capability at both high charge and discharge rates further promotes its applications for large current demands, such as electric and hybrid electric vehicles.

Acknowledgements

This work is financially supported by the sub-project "Exploration of novel cathode materials for lithium ion battery as highly efficient energy storage", the project "Design and Research on the Key Technology of Photovoltaic Demonstration Base", and the Knowledge Innovation Program of the Chinese Academy of Sciences， and the Strategic Priority Research Program of the Chinese Academy of Sciences，grant No. XDA09040101.

Notes and references

[a] National Center for Nanoscience and Technology of China, Beijing 100190, P. R. China. E-mail: wgchu@nanoctr.cn (W. Chu); wanghf@nanoctr.cn (H. Wang); lfs@nanoctr.cn (L. Sun); Fax: +86 10 62656765; Phone: +86 10 82545612

[b] Institute of Physics, Chinese Academy of Sciences, Beijing 100190, P. R. China

[c] Department of Physics, Tsinghua University, Beijing 100084, P. R. China

† Electronic Supplementary Information (ESI) available: See DOI: 10.1039/b000000x/

1 K. Padhi, K. S. Nanjundaswamy and J. B. Goodenough, *J. Electrochem. Soc.,* 1997, **144**, 1188.

2 R. Malik, A. Abdellahi and G. Ceder, *J. Electrochem. Soc.,* 2013, **160**, A3179.

3 W. J. Zhang, *J. Power Sources*, 2011, **196,** 2962.

4 J. Chong, S. D. Xun, X. Y. Song, P. Ridgwaya, G. Liu and V. S. Battaglia, *J. Power Sources,* 2012, **200**, 67.

5 Y. S. Hu, Y. G. Guo, R. Dominko, M. Gaberscek, J. Jamnik and J. Maier, *Adv. Mater.,* 2007, **19**, 1963.

6 F. Cheng, S. Wang, A. H. Lu and W. C. Li, *J. Power Sources,* 2013, **229**, 249.

7 Y. M. Wu, Z. H. Wen and J. H. Li, *Adv. Mater.*, 2011, **23**, 1126.

8 X. L. Wu, L. Y. Jiang, F. F. Cao, Y. G. Guo and L. J. Wan, *Adv. Mater*., 2009, **21**, 2710.

9 F. Q. Cheng, W. Wan, Z. Tan, Y. Y. Huang, H. H. Zhou, J. T. Chen and X. X. Zhang, *Electrochimica Acta*, 2011, **56**, 2999.

10 A. Vu and A. Stein, *J. Power Sources*, 2014, **245**, 48.

11 S. W. Oh, S. T. Myung, S. M. Oh, K. H. Oh, K. Amine, B. Scrosati and Y. K. Sun, *Adv. Mater*., 2010, **22**, 4842.

12 C. M. Doherty, R. A. Caruso and C. J. Drummond, *Energy Environ. Sci.*, 2010, **3**, 813.

13 M. Wagemaker, D. P. Singh, W. J. H. Borghols, U. Lafont, L. Haverkate, V. K. Peterson and F. M. Mulder, *J. Am. Chem. Soc*., 2011, **133**, 10222.

14 R. Malik, D. Burch, M. Bazant and G. Ceder, *Nano Lett.*, 2010, **10**, 4123.

15 C. W. Sun, S. Rajasekhara, J. B. Goodenough and F. Zhou, *J. Am. Chem. Soc.*, 2011, **133**, 2132.

16 W. Dreyer, J. Jamnik, C. Guhlke, R. Huth, J. Moškon and M. Gaberšček, *Nat. Mater.*, 2010, **9**, 448.

17 J. A. Gerbec, D. Morgan, A. Washington and G. F. Strouse, *J. Am. Chem. Soc.*, 2005, **127**, 15791.

18 S. L. Yang, X. F. Zhou, J. G. Zhang and Z. P. Liu, *J. Mater. Chem.*, 2010, **20**, 8086.

19 K. T. Lee and J. Cho, *Nano Today*, 2011, **6**, 28.

20 H. M. Xie, R. S. Wang, J. R. Ying, L. Y. Zhang, A. F. Jalbout, H. Y. Yu, G. L. Yang, X. M. Pan and Z. M. Su, *Adv. Mater.*, 2006, **18**, 2609.

21 J. B. Goodenough and K. S. Park, *J. Am. Chem. Soc.*, 2013, **135**, 1167.

22 D. Morgan, A. V. Ven and G. Ceder, *Electrochem. Solid-State Lett.*, 2004, **7**, A30.

23 P. Axmann, C. Stinner, M. W. Mehrens, A. Mauger, F. Gendron and C. M. Julien, *Chem. Mater.*, 2009, **21**, 1636.

24 J. J. Chen and M. S. Whittingham, *Electrochem. Commun.*, 2006, **8**, 855.

25 K. M. Ø. Jensen, M. Christensen, H. P. Gunnlaugsson, N. Lock, E. D. Bøjesen, T. Proffen and B. B. Iversen, *Chem. Mater.*, 2013, **25**, 2282.

26 B. Ellis, W. H. Kan, W. R. M. Makahnouk and L. F. Nazar, *J. Mater. Chem.*, 2007, **17**, 3248.

27 X. Qin, J. Wang, J. Xie, F. Z. Li, L. Wen and X. H. Wang, *Phys. Chem. Chem. Phys.*, 2012, **14**, 2669.

28 J. M. Tarascon, N. Recham, M. Armand, J. N. Chotard, P. Barpanda, W. Walker and L. Dupont, *Chem. Mater*., 2010, **22**, 724.

29 S. Y. Chung, J. T. Bloking and Y. M. Chiang, *Nat. Mater.*, 2002, **1**, 123.

30 F. Omenya, N. A. Chernova, S. Upreti, P. Y. Zavalij, K. W. Nam, X. Q. Yang and M. S. Whittingham, *Chem. Mater.*, 2011, **23**, 4733.

31 M. Vujković, D. Jugović, M. Mitrić, I. Stojkovica, N. Cvjetićanin and S. Mentus, *Electrochimica Acta*, 2013, **109**, 835.

32 M. Wagemaker, B. L. Ellis, D. Lützenkirchen-Hecht, F. M. Mulder and L. F. Nazar, *Chem. Mater.*, 2008, **20**, 6313.

33 B. Rehani, P. B. Joshi, K. N. Lad and A. Pratap, *Indian J. Pure & Appl. Phys.*, 2006, **44**, 157.

34 I. D. Brown, *Chem. Soc. Rev.*, 1978, **7**, 359.

35 M. Nespolo, G. Ferraris and H. Ohashi, *Acta Cryst.*, 1999, **B55**, 902.

36 J. J. Chen, S. J. Wang and M. S. Whittingham, *J. Power Sources*, **174**, 442.

37 F. Brochu, A. Guer, J. Trottier, M. Kope, A. Mauger, H. Groult, C.M. Julien and K. Zaghib, *J. Power Sources*, 2012, **214**, 1.

38 H. Zhang, Y. H. Tang, J. Q. Shen, X. G. Xin, L. X. Cui, L. J. Chen, C. Y. Ouyang, S. Q. Shi and L. Q. Chen, *Appl. Phys. A*, 2011, **104**, 529.

RSC advances

39 S. Y. Chung, S. Y. Choi, S. Lee and Y. C. Ikuhara, *Phys. Rev. Lett.*, 2012, **108**, 195501.

40 M. S. Islam, D. J. Driscoll, C. A. J. Fisher and P. R. Slater, *Chem. Mater*., 2005, **17**, 5085.

41 J. Lee, W. Zhou, J. C. Idrobo, S. J. Pennycook and S. T. Pantelides, *Phys. Rev. Lett.*, 2011, **107**, 085507.

42 S. Y. Chung, S. Y. Choi, T. Yamamoto and Y. Ikuhara, *Angew. Chem. Int. Ed.*, 2009, **48**, 543.

43 S. P. Badi, M. Wagemaker, B. L. Ellis, D. P. Singh, W. J. H. Borghols, W. H. Kan, D. H. Ryan, F. M. Mulder and L. F. Nazar, *J. Mater. Chem.*, 2011, **21**, 10085.

44 S. Hamelet, P. Gibot, M. C. Cabanas, D. Bonnin, C. P. Grey, J. Cabana, J. B. Leriche, J. R. Carvajal, M. Courty, S. Levasseur, P. Carlach, M. V. Thournout, J. M. Tarascon and C. Masquelier, *J. Mater. Chem.*, 2009, **19**, 3979.

45 J. J. Chen and J. Graetz, *ACS Appl. Mater. Interfaces*, 2011, **3**, 1380.

46 K. M. Ø. Jensen, H. P. Gunnlaugsson, M. Christensen and B. B. Iversen, *Hyperfine Interact*, 2013, **s10751**, 0992.

47 B. Hannoyer, A. A. M. Prince, M. Jean, R. S. Liu and G. X. Wang, *Hyperfine Interact*, 2006, **s10751**, 9354.

48 C. M. Julien, K. Zaghib, A. Mauger and Henri Groult. *Adv. Chem. Eng. Sci.*, 2012, **2**, 321.

49 K. Zaghib, J. Trottier, A. Mauger, H. Groult and C. M. Julien, *Int. J. Electrochem. Sci.*, 2013, **8**, 9000.

50 M. Y. Cho, K. B. Kim, J. W. Lee, H. Kim, H. Kim, K. Kang and K. C. Roh, *RCS Advances*, 2013, **3**, 3421.

51 B. Jin and H. B. Gu, *Solid State Ionics*, 2008, **178**, 1907.

52 X. L. Wu, Y. G. Guo, J. Su, J. W. Xiong, Y. L. Zhang and L. J. Wan, *Adv. Energy Mater.*, 2013, **3**, 1155.

53 K. Dokko, S. Koizumi, H. Nakano and K. Kanamura, *J. Mater. Chem.*, 2007, **17**, 4803.

54 X. M. Liu, P. Yan, Y. Y. Xie, H. Yang, X. D. Shen and Z. F. Ma, *Chem. Comm.*, 2013, **49**, 5396.

55 L. Wang, X. M. He, W. T. Sun, J. L. Wang, Y. D. Li and S. S. Fan, *Nano Lett.*, 2012, **12**, 5632.

56 B. Kang and G. Ceder, *Nature*, 2009, **458**, 190.

57 J. Y. Song and M. Z. Bazant, *J. Electrochem. Soc.*, 2013, **160**, A15.

58 Y. Zhao, L. L. Peng, B. R. Liu, G. H. Yu, Nano letters, 2014, **14**, 2849.

59 H. B. Shu, X. Y. Wang, W. C. Wen, Q. Q. Liang, X. K. Yang, Q. L. Wei, B. A. Hu, L. Liu, X. Liu, Y. F. Song, M. Zho, Y. S. Bai, L. L. Jiang, M. F. Chen, S. Y. Yang, J. L. Tan, Y. Q. Liao and H. M. Jiang, *Electrochimica Acta*, 2013, **89**, 479.

60 Y. Wang and G. Z. Cao. *Adv. Mater.*, 2008, **20**, 2251.

61 S. Y. Chung, S. Y. Choi, T. Yamamoto and Y. Ikuhara, *Phys. Rev. Lett.*, 2008, **100**, 125502.

62 F. Omenya, N. A. Chernova, Q. Wang, R. B. Zhang and M. S. Whittingham, *Chem. Mater.*, 2013, **25**, 2691.

63 S. Hamelet, M. C. Cabanas, L. Dupont, C. Davoisne, J. M. Tarascon and C. Masquelier, *Chem. Mater.*, 2011, **23**, 32.

64 K. Zaghib, A. Mauger, J. B. Goodenough, F. Gendron and C. M. Julien, *Chem. Mater.*, 2007, **19**, 3740.